Creation of a mixed-mode fracture network at meso-scale through hydraulic fracturing and shear stimulation

Authors:

Martin Schoenball[1], Jonathan B. Ajo-Franklin[2,1], Doug Blankenship[3], Chengping Chai[4], Patrick Dobson[1], Timothy Kneafsey[1], Hunter A. Knox[5], Monica Maceira[4], Michelle C. Robertson[1], Parker Sprinkle[5], Christopher Strickland[5], Dennise Templeton[6], Paul C. Schwering[3], Craig Ulrich[1], Todd Wood[1] and the EGS Collab Team[*]

[*] T. Baumgartner, K. Beckers, A. Bonneville, L. Boyd, S. Brown, J.A. Burghardt, Y. Chen, B. Chi, K. Condon, P.J. Cook, D. Crandall, T. Doe, C.A. Doughty, D. Elsworth, J. Feldman, Z. Feng, A. Foris, L.P. Frash, Z. Frone, P. Fu, K. Gao, A. Ghassemi, Y. Guglielmi, B. Haimson, A. Hawkins, J. Heise, C. Hopp, M. Horn, R.N. Horne, J. Horner, M. Hu, H. Huang, L. Huang, K.J. Im, M. Ingraham, E. Jafarov, R.S. Jayne, S.E. Johnson, T.C. Johnson, B. Johnston, K. Kim, D.K. King, J. Knox, D. Kumar, M. Lee, K. Li, Z. Li, P. Mackey, N. Makedonska, E. Mattson, M.W. McClure, J. McLennan, C. Medler, R.J. Mellors, E. Metcalfe, J. Moore, C.E. Morency, J.P. Morris, T. Myers, S. Nakagawa, G. Neupane, G. Newman, A. Nieto, C.M. Oldenburg, T. Paronish, R. Pawar, P. Petrov, B. Pietzyk, R. Podgorney, Y. Polsky, J. Pope, S. Porse, J.C. Primo, C. Reimers, B.Q. Roberts, W. Roggenthen, J. Rutqvist, D. Rynders, V. Sesetty, C.S. Sherman, A. Singh, M.M. Smith, H. Sone, E.L. Sonnenthal, F.A. Soom, C.E. Strickland, J. Su, J.N. Thomle, V.R. Tribaldos, N. Uzunlar, A. Vachaparampil, C.A. Valladao, W. Vandermeer, G. Vandine, D. Vardiman, V.R. Vermeul, J.L. Wagoner, H.F. Wang, J. Weers, N. Welch, J. White, M.D. White, P. Winterfeld, S. Workman, H. Wu, Y.S. Wu, E.C. Yildirim, Y. Zhang, Y.Q. Zhang, Q. Zhou, M.D. Zoback

Affiliations

[1] Lawrence Berkeley National Laboratory, Berkeley, California

[2] Rice University, Houston, Texas

[3] Sandia National Laboratories, Albuquerque, New Mexico

[4] Oak Ridge National Laboratory, Oak Ridge, Tennessee

[5] Pacific Northwest National Laboratory, Richland, Washington

[6] Lawrence Livermore National Laboratory, Livermore, California

Key points

· Mesoscale hydraulic fracturing in crystalline rock observed with multi-geophysical sensor array at close proximity

· Created fracture network consists of multi-strand hydraulic fractures and reactivated pre-existing structures

· Hydraulic fracture growth is strongly influenced by rock fabric, pre-existing fractures, and stress heterogeneities

Abstract

Enhanced Geothermal Systems could provide a substantial contribution to the global energy demand if their implementation could overcome inherent challenges. Examples are insufficient created permeability, early thermal breakthrough, and unacceptable induced seismicity. Here we report on the seismic response of a meso-scale hydraulic fracturing experiment performed at 1.5 km depth at the Sanford Underground Research Facility. We have measured the seismic activity by utilizing a novel 100 kHz, continuous seismic monitoring system deployed in six 60 m-length monitoring boreholes surrounding the experimental domain in 3-D. The achieved location uncertainty was on the order of 1 m, and limited by the signal-to-noise ratio of detected events. These uncertainties were corroborated by detections of fracture intersections at the monitoring boreholes. Three intervals of the dedicated injection borehole were hydraulically stimulated by water injection at pressures up to 33 MPa and flow rates up to 5 L/min. We located 1933 seismic events during several injection periods. The recorded seismicity delineates a complex fracture network comprised of multi-strand hydraulic fractures and shear-reactivated, pre-existing planes of weakness that grew unilaterally from the point of initiation. We find that heterogeneity of stress dictates the outcome of hydraulic stimulations, even when relying on theoretically well-behaved hydraulic fractures. Once hydraulic fractures intersected boreholes, the boreholes acted as a pressure relief and fracture propagation ceased. In order to create an efficient sub-surface heat exchanger, production boreholes should not be drilled before the end of hydraulic stimulations.

1. Introduction

Geothermal heat can be a reliable source of clean energy that is able to provide baseload capacity. Enhanced geothermal systems (EGS) promise the availability of geothermal energy anywhere if we only drilled to sufficient depth and were able to create an efficient subsurface heat exchanger to accommodate a sustainable circulation of fluid between injection and production boreholes (Tester et al., 2006). Creating such a heat exchanger has been a long-standing challenge (Doe et al., 2014; Grant, 2015) and one that needs to balance the economic need for high fluid flow rate, avoiding hydraulic short circuits and preemptive thermal breakthrough, and undesirable levels of induced seismicity.

Past efforts to create full-scale EGS have suffered from insufficient artificial permeability created through their attempts at shear stimulation, as observed at the Soultz-sous-Forêts, France site (Genter et al., 2010) or earlier at the Fenton Hill pilot in New Mexico, USA (Norbeck et al., 2018). It has been proposed to create EGS through primarily tensile hydraulic fractures (Jung, 2013) or through specifically targeting the creation of a fracture network that is based on a mix of newly created hydraulic fractures and utilization of pre-existing structures that are to be reactivated in shear (McClure & Horne, 2014). Given the success of the modern unconventional oil and gas industry in creating engineered permeability for hydrocarbon production, researchers are hoping to harness these same technologies for EGS including the use of proppants, zonal isolation, and designer fracture networks.

A critical component of EGS development is to mitigate the induced seismicity risk associated with hydraulic fracturing and potential reactivation of faults at seismogenic depth (Diehl et al., 2017; Ellsworth et al., 2019; Häring et al., 2008). It remains poorly understood exactly how high-pressure fluid injections influence the state of stress and the likelihood of seismogenic slip of nearby faults (Walsh & Zoback, 2016). Lastly, creating an underground heat exchanger must avoid creating early thermal breakthrough between production and injection boreholes (Parker, 1999), which can be caused by excessive flow channeling. Some of the open questions upon which EGS success depends are: How can we control the level of seismic activity and the largest events being induced? Can we utilize hydraulic fracturing techniques to create a suitable fracture network? What are reasonable thermal recovery factors for the seismically imaged EGS reservoir volume, and how can these be increased? What is the role of pre-existing fractures, rock features and stress heterogeneity in these processes?

The complexity of the required advancements of EGS technology, the high costs of performing full-scale experiments and the difficulty of adequately instrumenting test sites at typical depths greater than 3 km are driving a recent renaissance of underground mesoscale experiments i.e. at dimensions of 10s to 100s of meters. Such experiments provide the realism of a heterogeneous rock body, in contrast to laboratory studies on core samples, while simultaneously offering the potential of significantly lower cost

77 with higher instrumentation density than a full reservoir-scale pilot study. These intermediate scale
78 experiments try to strike a balance between easy access that allows for dense instrumentation and novel
79 sensor deployments, size of the experimental volume, and relevant stress and temperature conditions.
80 Several experiments are being conducted in underground laboratories in crystalline rock that were
81 originally targeted for nuclear waste storage research such as at the Äspö Hard Rock Laboratory, Sweden
82 (Kwiatek et al., 2018; Zang et al., 2017) or at the Grimsel Test Site, Switzerland (Amann et al., 2018;
83 Gischig et al., 2018; Villiger et al., 2019). Other experiments used opportune mining environments to
84 learn about the processes involved in fracturing from in-situ observations (Jeffrey et al., 2009; Kwiatek et
85 al., 2011; Dresen et al., 2019). An advantage of deep underground mining environments in contrast to
86 shallow tests is the availability of higher *in situ* stress conditions at relatively short drilling depths.
87 The EGS Collab project strives to improve our understanding of creating subsurface heat exchangers
88 through densely monitored mesoscale stimulation experiments at relevant depth. The project is laid out as
89 an integrated effort to combine experimental and modelling work applied to EGS development. We
90 selected a site at the Sanford Underground Research Facility, located in Lead, South Dakota formerly
91 known as the Homestake Gold Mine (Kneafsey et al., 2019; Dobson et al., 2020). The first suite of
92 experiments is being conducted in the West Drift of the 4850 ft-level, approximately 1.5 km below the
93 surface. The site is in the immediate vicinity of prior experiments conducted as part of the kISMET
94 project, where permeability creation through hydraulic fracturing was studied prior to EGS Collab
95 (Oldenburg et al., 2017). A testbed consisting of eight sub-horizonal boreholes of 60 m length was
96 designed to study the creation and function of a subsurface heat exchanger based on the utilization of
97 hydraulic fractures designed to connect an injection-production borehole doublet. The monitoring
98 boreholes were equipped with a wide array of sensors ranging from passive and active seismic through
99 fiber-optics to electrical resistivity and in-situ displacement sensors. Here we report on the seismic
100 response of the metamorphic rock mass to a series of stimulation experiments and the creation of a
101 complex reservoir comprised of hydraulic fractures and reactivated natural fractures. First, we summarize
102 prior baseline characterization and describe the instrumentation of the testbed. Then we describe the
103 injection tests and seismic observations in chronological order before we discuss all tests together and put
104 them in context with complementary observations enabled by the multi-modal instrumentation. We close
105 with a comparison of our observations to other mesoscale experiments.
106
107 **2. Experiment overview**
108 Experiment 1 of the EGS Collab Project benefitted from a thorough characterization of prior experiments
109 near the site such as from the kISMET project (Oldenburg et al., 2017). The experiment is embedded in a
110 host rock of carbonate-rich, quartz-bearing phyllite of the upper Poorman formation (Caddey et al., 1991).

This metamorphic rock is strongly foliated and as a result has a highly anisotropic mechanical response (Frash et al., 2019; Vigilante et al., 2017). The anisotropy also holds for the larger scale as revealed through baseline electrical resistivity tomography (ERT) by Johnson et al. (2019) who imaged a 10 m-scale fold running through the rock volume of our testbed. A discrete fracture network model was developed based on image logs, core and fracture isolation flow tests (Neupane et al., 2019; Roggenthen & Doe, 2018; Ulrich et al., 2018). A high-resolution cross-well seismic tomography campaign was conducted to collect compressional- and shear-wave velocities, v_p and v_s of the testbed prior to stimulation (Schwering et al., 2018). The data were processed and initially inverted for isotropic first-arrival traveltime tomographic imaging, and the results were utilized for elastic moduli calculations (Linneman et al., 2018). Average velocity values in the best-constrained region of the tomographic models were approximately 6,000 and 3,200 m/s for v_p and v_s, respectively. These data have been utilized for anisotropic adjoint-state first-arrival traveltime tomography and anisotropic elastic-waveform inversion methods to refine the initial velocity models (Gao et al., 2020). The stress field has been characterized as normal faulting through hydraulic fracturing tests during the kISMET project (Wang et al., 2017). Furthermore, it was necessary to consider perturbations to the tectonic stress field accounting for the excavation damage zone, the perturbation by the presence of a free surface at the drift (mine tunnel), and lastly the excavation and ventilation history and resulting thermal stresses. The West Drift was excavated starting in 1949, flooded in 2007 after the mining activity ceased and pumped dry in 2009 to enable access for scientific experiments (Lesko, 2015). The natural temperature of the rock is about 38˚C and the drift is circulated with fresh air cooling it to an ambient temperature of about 20˚C. To assess the impact of this history on the planned stimulation activity, Fu et al. (2018) and White et al. (2018) performed a numeric analysis of thermal stresses in the host rock and their implication on fracture propagation. They predicted that a newly created hydraulic fracture would preferentially grow towards the drift. This finding was incorporated in the experimental design by placing the production borehole between the injection borehole and the drift (Figure 1).

2.1. Testbed design and monitoring array

To monitor the coupled mechanical, thermal, and hydrogeologic processes occurring during stimulation, the testbed was designed to surround the experimental volume in 3-D. The testbed consists of eight boreholes of about 60 m length and 96 mm diameter, drilled from a single drift at 1480 m below the surface (Figure 1). Two of these boreholes were designated as the injection (E1-I) and production (E1-P) boreholes for the purposes of the stimulation and flow experiments. The other six boreholes were instrumented with a multi-modal instrument string that included a fiber optic cable for distributed sensing of temperature (DTS), strain (DSS) and acoustic (DAS) signals, electrode strings for ERT, thermistors,

piezoelectric seismic sources for continuous active seismic source monitoring (CASSM) (Daley et al., 2007), hydrophones, and accelerometers. The borehole locations were identified using laser survey mapping of the borehole wellheads in the drift and gyro log surveys of the borehole trajectories. All sensors and active sources were affixed to a 1-inch PVC pipe to allow conveyance into the sub-horizontal boreholes. The sensor strings were grouted to seal the boreholes and provide mechanical coupling. Two SIMFIP *in situ* displacement sensors (Guglielmi et al., 2014) were deployed in both experimentation boreholes E1-I and E1-P. In this paper we focus on the continuous passive seismic recordings and use the active seismic, DTS, and SIMFIP sensors for verification.

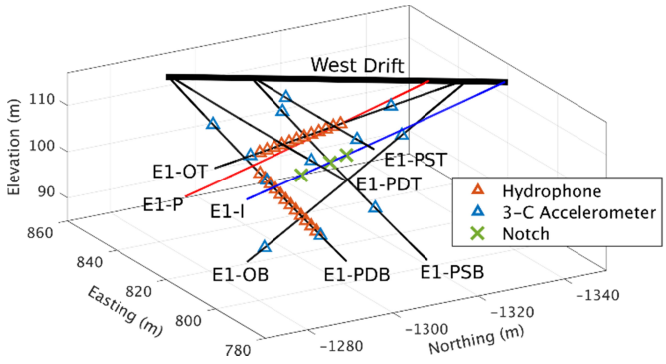

Figure 1: Network of hydrophones and accelerometers around the injection (E1-I) and production (E1-P) boreholes. Notches are at the intervals selected for fluid injection. The orientation of stimulation and production boreholes is approximately parallel to S_{hmin}.

For continuous passive seismic recording we used two independent acquisition systems, recording at 4 kHz and 100 kHz respectively. The data recorded at 4 kHz sampling rate (OYO Geores) was deemed to be temporally undersampled for the types of signals generated during stimulation and is not discussed any further. The 100 kHz recording system utilized a 64-channel, 24 bit analog/digital converter (Data Translation, VibBox-64). Two hydrophone strings were deployed in boreholes E1-OT and E1-PDB. Each string consists of twelve hydrophones (High Tech, HTI-96-Min) at 1.75 m spacing. Additionally, twelve 3-component piezoelectric accelerometers (PCB 356B18) were deployed in the boreholes and connected to the 100 kHz recording unit.

The hydrophones are reported to have a relatively flat frequency response up to about 35 kHz (Figure 2a) although the effect of cementation has not been quantified. The accelerometers, which were potted in stainless steel housings for protection, are specified to have a flat response of 1 V/g up to 5 kHz frequency (± 10 %) and with a resonance frequency >20 kHz. Since the recorded seismic signals were at frequencies higher than anticipated and outside of the accelerometer's manufacturer specifications we obtained a frequency response curve using a high frequency, electrodynamic shake table (Spektra SE-09) for one accelerometer. As shown in Figure 2a, the frequency response becomes significantly non-linear

above about 5 kHz with several resonance frequencies at about 10 kHz and higher. Unfortunately, the recorded seismicity had the most seismic energy in the resonance range around 10 kHz (Figure 2b and c). This is resolved well by the hydrophones as shown by the spectrogram of an example event (Figure 2c). For the same event, the accelerometers recorded energy well above 10 kHz which we attribute to sensor resonances (Figure 2b). Unfortunately, this precludes us from quantitively using the amplitude information recorded by the accelerometers for measurement of magnitudes and moment tensors.

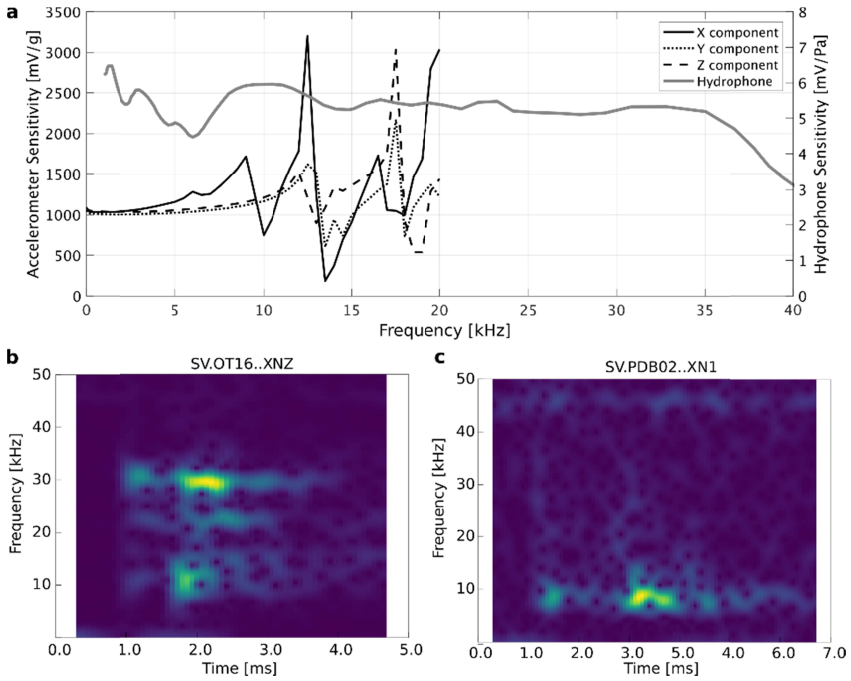

Figure 2: (a) Frequency response of deployed accelerometers (as measured in the lab) and hydrophones (from the manufacturer specifications sheet). (b) Spectrograms of a sample event on z-component of accelerometer OT16 and (c) of hydrophone PDB02.

2.2. Data processing

We developed an automated near-realtime processing flow based on the Python package ObsPy (Krischer et al., 2015). Files of 32 s duration were processed sequentially. Between files there was a gap of about 1.5 s with no data due to computational overhead. Seismic signals were contaminated by electrical spikes from the recording system, active seismic shots about every 0.8 s, and sensor cross-talk from the ERT system that uses cables collocated with the passive seismic sensor cables. These noise signals were removed using the active source trigger signal, or based on waveform features detecting maximum amplitudes within 3 samples. The active sources produced waveforms that cover about 2.5% of the time series that is not useable for passive seismic analysis.

Events were detected with a standard STA/LTA routine (Allen, 1978) where we require at least 10 individual traces to trigger to detect an event. First arrival times were then refined using an AIC picker implemented in the package PhasePAPy (Chen & Holland, 2016). If at least 5 P-wave picks were obtained from one event they were passed on to Hypoinverse (Klein, 2014). We use a version of Hypoinverse that is modified to accommodate the time precision of 10^{-5} s needed for our application. This processing workflow is implemented on an 8-core workstation and is able to handle about 1 triggered event per second. During periods of peak activity this level may be far exceeded however, leading to a backlog of events to be processed. In later processing steps we manually reviewed and refined all automatic P-wave picks and added S-wave picks where possible.

We used a simplified velocity model with a single P-wave velocity of 5900 m/s and a v_p/v_s ratio of 1.78. This velocity was determined by locating the active sources and then minimizing the misfits between their known location and our determined location while varying v_p. The selected P-wave velocity falls within the range of v_p values observed from the seismic crosswell survey of the testbed (Schwering et al., 2018). In the following section we quantify the location uncertainty obtained with our processing applied to the testbed. In normal earthquake monitoring settings, the location uncertainty is governed by the uncertainty in first break picking and unknown complexity of the applied velocity model. In our application a third component is the uncertainty in the location of sensors. Our working assumption is that borehole trajectories are generally known with better than 1 m accuracy. The location of sensors along the borehole is assumed to be known to 0.05 m or better and represent no relevant source of error.

During the experiments the active seismic sources (CASSM) were operated semi-continuously to obtain a velocity model epoch every 15 minutes. We used these sources to separately quantify the location precision and accuracy of our automatic processing. We automatically determined the P-wave first arrivals and locations as described above. We computed the accuracy of our locations as the vector between the mean determined location and the assumed location of the CASSM sources. Accuracy was determined to be better than 1.5 m (Figure 3a). It is important to note that the assumed location of the CASSM sources do contain their own error related to the uncertainty of the borehole trajectories as discussed above. We noticed a systematic deviation between the determined and assumed location of the sources as we go deeper along borehole E1-PST. Based on further evidence from inversion of ERT and active seismic data, it is assumed that the trajectory of this borehole has a systematic error on the order of 1˚, translating into errors of up to 1 m at the bottom of that borehole. The location precision for each source is obtained from the largest component of the ellipsoid that contains 95 % of determined locations. We found the location precision to be better than 0.8 m and typically better than 0.5 m (Figure 3a and c). Most of the recorded seismic events have a much lower signal-to-noise ratio than the active sources, so precision of our seismic event locations is limited by the accuracy of picking the first arrivals on a

sufficient number of sensors. In Figure 3b we plot the fraction of events with a formal location precision better than a given location uncertainty. We find that for 80 % of events the location precision is better than 2.0 m. Because the monitoring array is distributed in 3-D around the events, there is no significant difference between the horizontal and vertical precision.

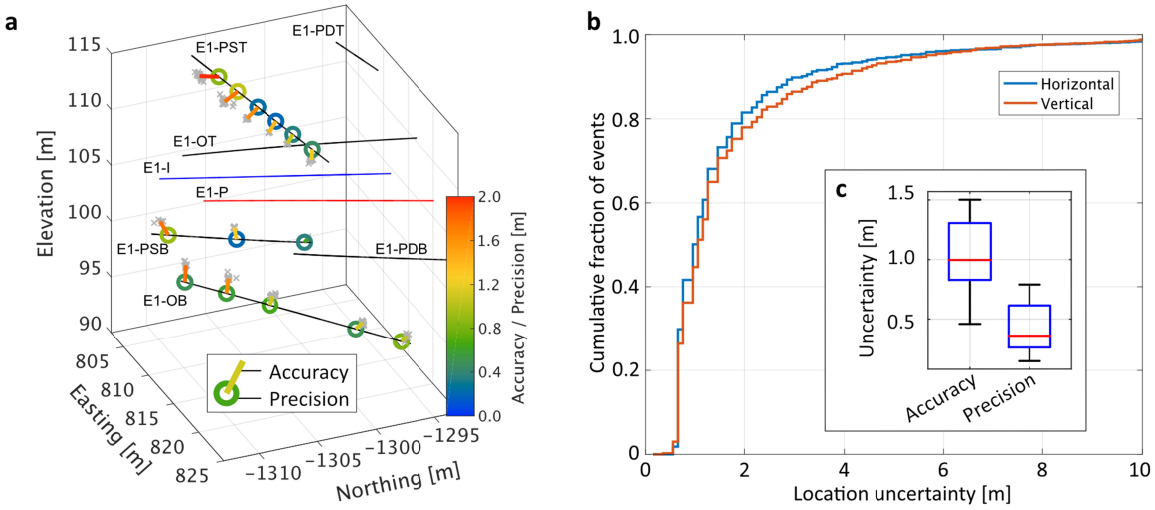

Figure 3: (a) Location uncertainty of CASSM sources quantified as accuracy (color of lines between located sources [gray] and circles) and precision (color of circles). Note the systematic increase of the offset between the assumed and determined locations of sources in the PST well. (b) Distribution of formal location precision of hypocenters inverted from P and S arrivals. (c) Boxplots of the distributions of accuracy and precision for the determined CASSM source locations as plotted in (a).

3. Results

During May and December of 2018, hydraulic stimulations were conducted at three locations in borehole E1-I at depths of 128 ft (39.0 m), 142 ft (43.3 m) and 164 ft (50.0 m), respectively. For each stimulation a 1.8 m long interval between two straddle packers was pressurized in E1-I (Ingraham et al., 2018). Optical and acoustic televiewer images of the injection intervals prior to stimulation are shown in Figure 4. During well completion, a notch was made at each of the locations that was intended to guide the initiation of a hydraulic fracture (Morris et al., 2018). All injections occurred with non-potable industrial-grade water. The first injection occurred at the 142 ft notch in E1-I but was quickly abandoned when no fracture breakdown was observed at the anticipated pressure level. Furthermore, the SIMFIP in-situ displacement sensor initially indicated shear deformation, and the intentions for this experiment were to study hydraulic fracturing rather than shear fracturing.

In the following sections we interpret the cloud of seismic events structurally based on planar fracture features. In a 3-D viewer, we plot only well-located events with a location uncertainty better than 1.5 m.

We select events that appear to be associated with a planar feature that we interpret to be a fracture. The position and orientation of fractures were determined through principal component analysis. We compute the covariance matrix of all earthquake hypocenters associated with an interpreted fracture. The location and orientation of the fracture is then obtained from its eigenvector and eigenvalues, respectively. The dimensions of the activated fracture sections are obtained from the major and intermediate axes of the ellipsoid defined by the hypocenters and scaled to include the 95 % confidence interval if events followed a χ^2 distribution in space. We identified 10 fractures this way as shown in Figure 5.

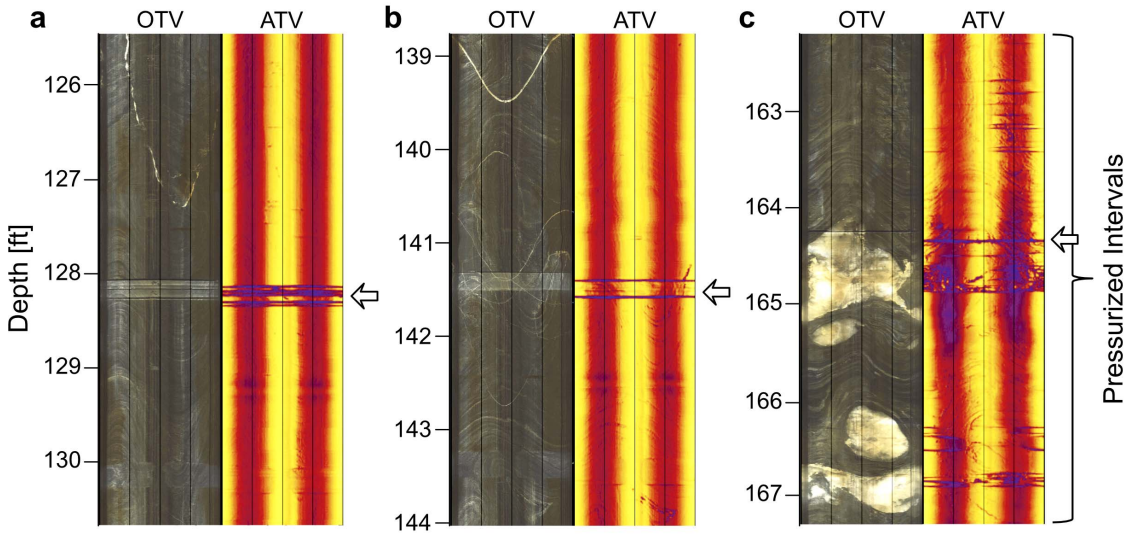

Figure 4: Optical (OTV, left) and acoustic (ATV, right) televiewer images of the three stimulated intervals at (a) 128 ft, (b) 142 ft and (c) 164 ft. The televiewer images were obtained prior to hydraulic stimulation and show the machined notches perpendicular to the borehole axis marked by arrows.

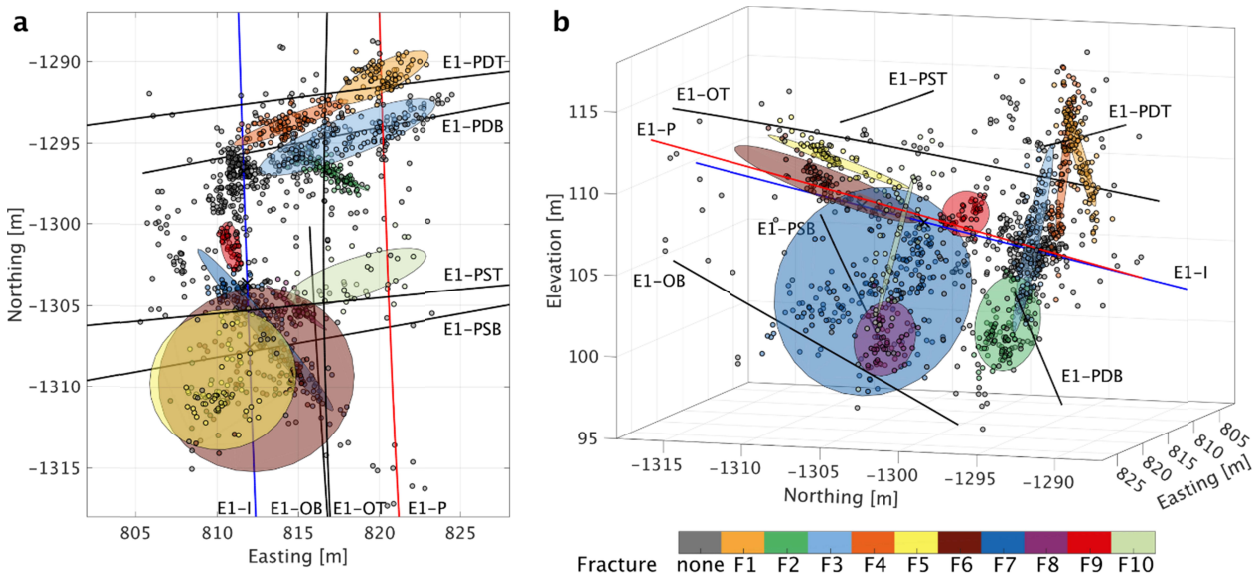

Figure 5: Interpreted fractures activated by the stimulations. Microseismic events are represented by small circles color-coded according to their corresponding fracture plane. Gray events were not associated with an identified fracture plane.

3.1. 164 ft stimulations, May 22 – 25, 2018

We relocated the straddle packer assembly to the 164 ft location in E1-I and began the first test on May 22, 2018 at 21:55 UTC by injection of water at 200 mL/min over a 10-minute period (Figure 6a). This test was designed to create a hydraulic fracture of 1.5 m nominal diameter. The nominal dimensions were calculated based on the assumption of a circular, penny-shaped crack. We recorded and located 36 seismic events during this period that formed a cloud of approximately 3 m in diameter around the injection interval. Our resolution is not sufficient to image a clear trend or structure in this cloud of seismic activity.

After overnight shut-in, the stimulation continued at a flow rate of 400 mL/min for about 60 min to enlarge the fracture to a nominal diameter of 5 m (Figure 6b). We initially observed seismicity in the same area as in the previous test. However, 10 minutes after reaching the maximum pressure, the seismicity began to migrate toward the injection well and slightly downward. After 30 minutes, seismic activity changed its migration pattern and grew predominantly upward, reaching the monitoring borehole E1-OT at about 19:29 UTC and migrating above it. At 19:34 UTC a temperature anomaly of +0.36 K was observed at 47 m depth in the E1-OT borehole from the DTS system. The DTS system records in 10 minute intervals, so the time of breakthrough was between 19:24 and 19:34 and in agreement with the arrival of seismic activity. The positive temperature anomaly was interpreted as being related to a Joule-

Thompson effect as the injected fluid pressure decreased upon entry into the grouted monitoring well (Zhang et al., 2018). Seismicity at the E1-OT borehole was relatively sparse; the closest event was located at about 45.5 m along its depth. Overall, seismicity developed in a fairly planar fashion with most seismicity associated with a single fracture F4 at a strike of about N75˚E. From that point on, the hydrophones and accelerometers deployed in E1-OT were exceedingly noisy, presumably due to water jetting into the borehole and causing direct vibrations to the sensor string. Elevated flow noise subsided after the injection tests but reappeared once a comparable hydraulic regime was reached. It was determined later that the grout in the boreholes did not seal effectively and several attempts to reseal the monitoring boreholes would follow.

After another overnight shut-in we resumed injection and increased the maximum flow rate to 5 L/min and injected until fracture breakthrough into the production borehole was observed (Figure 6c). Breakthrough in E1-P was evidenced by fluid outflow from the well collar and deformation recorded by the SIMFIP probe in the production borehole. Because of the much higher flow rate, and despite almost unchanged injection pressure, the seismicity rate was much higher than in previous injections, producing 280 events in about 20 minutes of injection. Only the largest events could be clearly located because of the ambiguity of associating wave trains for the bulk of smaller events (Figure 7). During that test, a second fracture F3 sub-parallel to the first fracture F4 became active. Further, fracture F2 with a strike of about N120˚E and with activity located below the other fractures became active as well.

The seismic cloud intersected with the production borehole at around 39.5 m depth. In a later test, video footage of fluid flowing into the production well was acquired using a downhole camera. We saw fluid jetting into the borehole at 39 m depth, which is consistent with the locations of the hydraulic fracture determined from the seismic events.

Following another overnight shut-in, two 1-hour long flow tests of up to 4.5 L/min flow rates were conducted on May 25, 2018. The first test injected water above fracture opening pressures for about 20 minutes. Although a volume comparable to the previous stimulation was injected only minor seismic activity with a total of 65 events was recorded (Figure 6d). The second flow test began after about 5 hours of shut-in and continued with moderate seismic activity at a flow rate of 3.7 L/min. After 20 minutes at that flow rate, it was increased to 4.5 L/min, the same used in the previous test. Activity on a new fracture (F1), detached from the previous activity, appeared. Interestingly, fracture F1 has a similar strike as the previously active hydraulic fractures but is dipping in the opposite direction at similarly steep angle. After shut-in, activity lingered on in this fracture much longer than observed after any of the previous injection tests (Figure 6e).

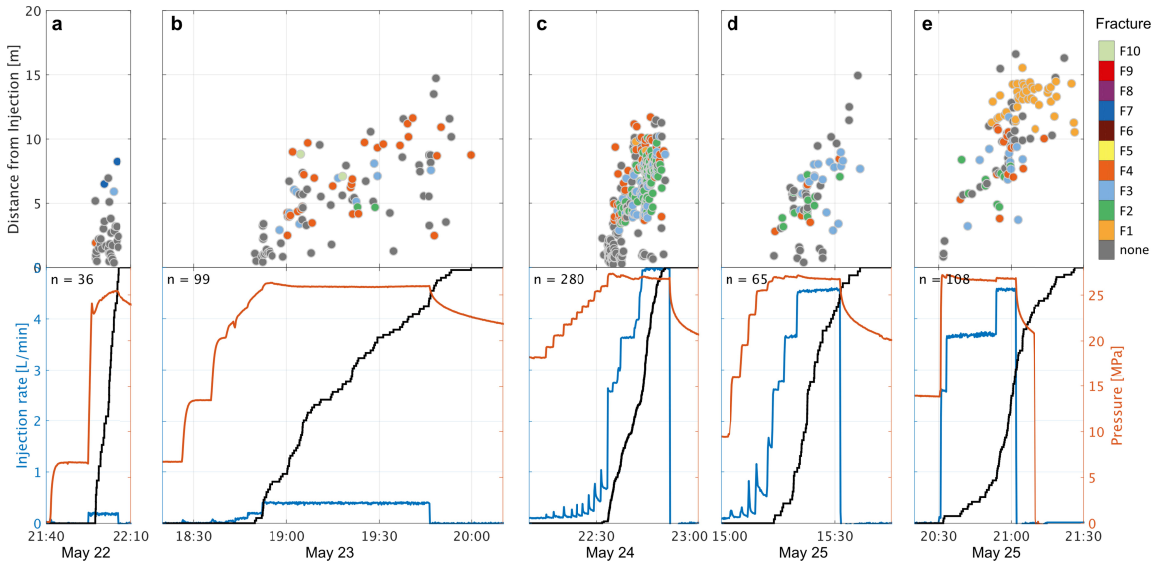

Figure 6: Overview of stimulations and flow tests at the 164 ft notch. Top panels: Distance of events from the injection. Events are colored based on their corresponding fracture (Figure 5), Bottom panels: Injection rate (blue), pressure (red) and cumulative number of events (black), normalized to fit the panel. The total number of events for each stage is printed in the top left corner.

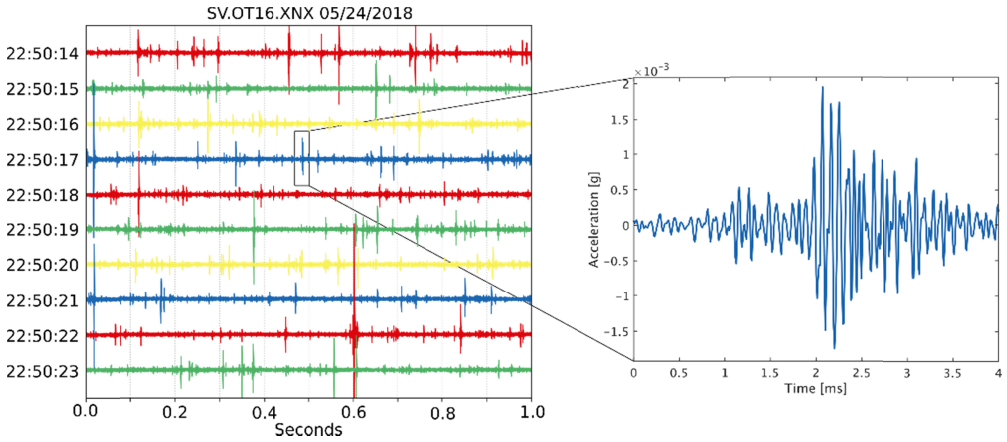

Figure 7: Data recorded at sensor OT16 during the injection at 5 L/min when the highest event rate was observed and just before breakthrough into E1-P. Each line represents 1 s of data for a total of 10 s displayed. Other sensors did provide signals of considerably smaller signal-to-noise ratio, thus yielding a much lower count of total located events.

3.2. Alternating stimulation in E1-P, June 25, 2018

After one month of experimental inactivity we performed an alternating stimulation with a first injection in E1-P at a location at 39 m depth, where the fracture breakthrough was detected previously. During two short injection pulses of about 4 minutes water was injected at up to 4.3 L/min. A total of 58 events were

recorded during that period, primarily limited to the hydraulic fracture F3 that intersected E1-P at the injection interval (Figure 8). At 17:55 UTC, towards the end of this first injection phase, we observed a thermal anomaly in borehole E1-PDB at 32.25 m depth. The injection was then reversed back to E1-I at the same location at the 164 ft notch as used during the May 22-25 injections. Injection pressures exceeded 30 MPa at injection rates up to 4 L/min. Seismic activity was mostly confined to the two deep hydraulic fracture strands F1 and F4 with considerable activity in F1, even after significant reductions in flow rate and injection pressure. This is consistent with the persisting seismicity observed after the May 25 injections.

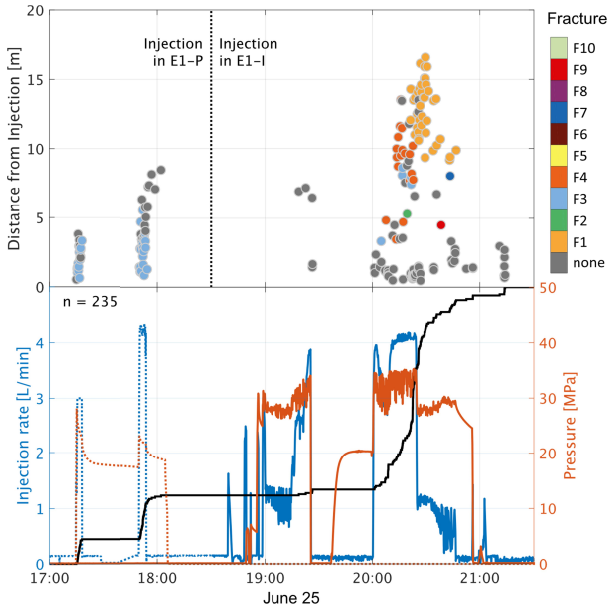

Figure 8: Overview of stimulations and flow tests on June 25, 2018 with injection into E1-P (dotted) and subsequent injection into E1-I (solid) at the 164 ft location. Injection rate (blue), pressure (red) and cumulative number of events (black), normalized to fit the panel.

3.3. 128 ft stimulation, July 19 & 20, 2018

The shallowest stimulated location at 128 ft was stimulated during July 19 & 20, 2018. During the first stimulation at a maximum injection rate of 400 mL/min fracture breakdown was inferred when injection pressures reached up to 27.9 MPa – thus significantly higher than observed during the initial stimulations at the 164 ft location. Sparse seismic activity began at pressures above 25 MPa. Unfortunately, the passive seismic system had an outage beginning at 17:44 UTC and no more data could be acquired during this test. After overnight shut-in, stimulation treatment continued on July 20 with injection rates up to 1.5 L/min and pressure of almost 30 MPa. During the periods of higher injection rate seismic activity increased (Figure 9).

Even though the maximum pressures were significantly higher than in stimulation treatments at the 164 ft location no hydraulic fracture was created. Instead a sub-horizontal cloud of seismicity was produced. Closer inspection revealed a set of two shallow dipping fractures. On July 20, at 21:32 a temperature anomaly of up to +0.7 K was detected through the DTS system at 24 m depth in borehole E1-OT. Although about 10 m away from located seismicity, this location is consistent with the sub-horizontal trend of fracture F5 if its trend would be extended towards the E1-OT borehole.

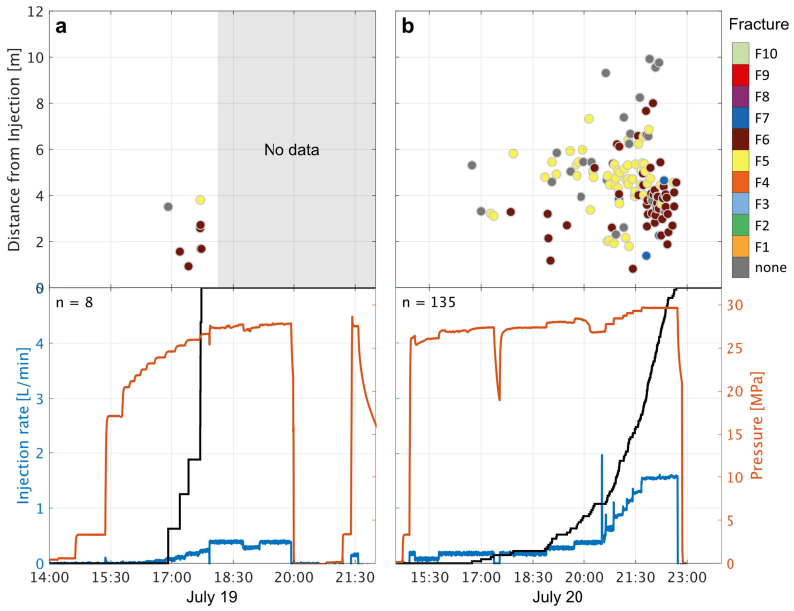

Figure 9: Overview of stimulations and flow tests at the 128 ft notch. Top panels: Distance of events from the injection. Events are colored based on their corresponding fracture, Bottom panels: Injection rate (blue), pressure (red) and cumulative number of events (black), normalized to fit the panel. The total number of events for each stage is printed in the top left corner.

3.4. 142 ft stimulation December 7, December 21 & 22, 2018

On December 7, 2018 we continued stimulation of the notch at 142 ft depth in E1-I, where the very first injection on May 21 was quickly abandoned. The interval was pressurized using a flow rate of 2.5 L/min to a pressure of 32 MPa where we observed fracture opening. Less than 2 min after reaching the fracture opening pressure a packer element burst and we had to cancel the stimulation (Figure 10a). After replacing the packer, a third attempt to stimulate the interval began on December 21, 2018. We increased the flow rate up to 5 L/min and observed the maximum pressure of 33.7 MPa, which reduced and stabilized at 32.7 MPa during fracture propagation (Figure 10b). The seismic response was vigorous with 426 events observed during this test. Seismicity grew along fractures F7 and F8 downward and towards E1-OB. During this test numerous thermal anomalies related to fracture hits were detected by the DTS

system in the monitoring boreholes. The first thermal signal was detected at 17:15 at 37.25 m depth in OB, corresponding to seismicity in F8. A second anomaly was detected at 19:30 at 32.25 m depth in OB, corresponding to fracture F7. For both thermal anomalies the closest seismicity projects within 1 m of the thermal anomaly detected by the DTS system.

Most seismic activity was confined to shear fracture F7 that was reactivated along a 10 m long segment. Fracture F9 became newly active and seismic activity grew sub-parallel to E1-I and in the opposite direction of F7. Both fractures appear to originate from the injection interval in E1-I and their reactivated sections grew one-sided away from the injection interval. The image log of E1-I does show several mineral-filled fractures near the machined notch (Figure 4) at 142 ft as well as a series of fractures at 146 ft. Two fractures identified on image logs have an orientation roughly matching the orientation of the reactivated fracture F7 (strike & dip of 138 & 78 vs. 140 & 85 for the logged fracture and F7, respectively). This feature corresponds to the Intermediate Fracture Zone as characterized by Neupane et al. (2019).

Very slowly and with only minor seismic activity a part of the seismic cloud grew towards E1-P with an orientation consistent with a hydraulic fracture (F10). This feature shares the same orientation as the hydraulic fractures that were created in May and connect the 164 ft notch with E1-P. Thermal anomalies were detected at 20:19 at 37.25 m depth in E1-OT and at 17:15 at 37.20 m depth in E1-OB. Several fracture intersections with E1-P were found within 0.5 m of 31.0 m depth using a downhole camera during the Dec 21 injection. These fracture intercepts align very well with the interpreted hydraulic fracture and confirm the orientation and location of the hydraulic fracture independently.

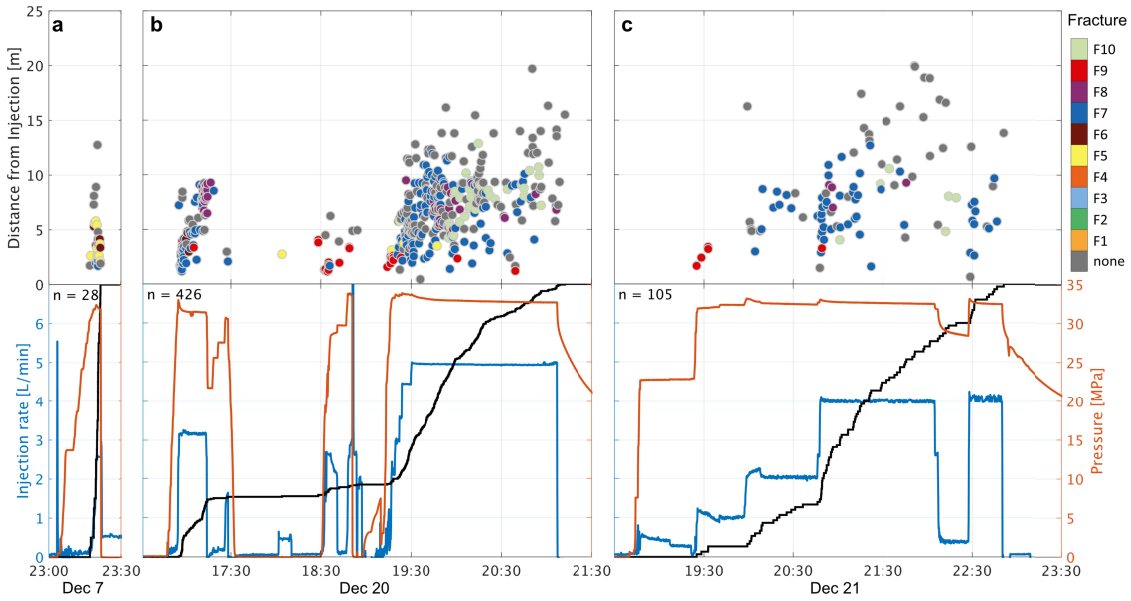

Figure 10: Overview of stimulations and flow tests at the 142 ft notch. Top panels: Distance of events from the injection. Events are colored based on their corresponding fracture, Bottom panels: Injection rate (blue), pressure (red) and cumulative number of events (black), normalized to fit the panel. The total number of events for each stage is printed in the top left corner.

4. Discussion

Several high-pressure fluid injections at the three notched locations in the borehole E1-I created a very diverse range of seismic responses. Stimulations at each injection interval produced significantly differing fracture propagation responses despite being located in the same rock type and separated only about 10 m in the same borehole (Figure 11). While we observed hydraulic fracturing when injecting at the 164 ft and 142 ft locations, seismic responses consistent with shear fracturing dominates the seismic activity at the 128 ft and 142 ft locations. Below we discuss the observed seismicity and complementary observations.

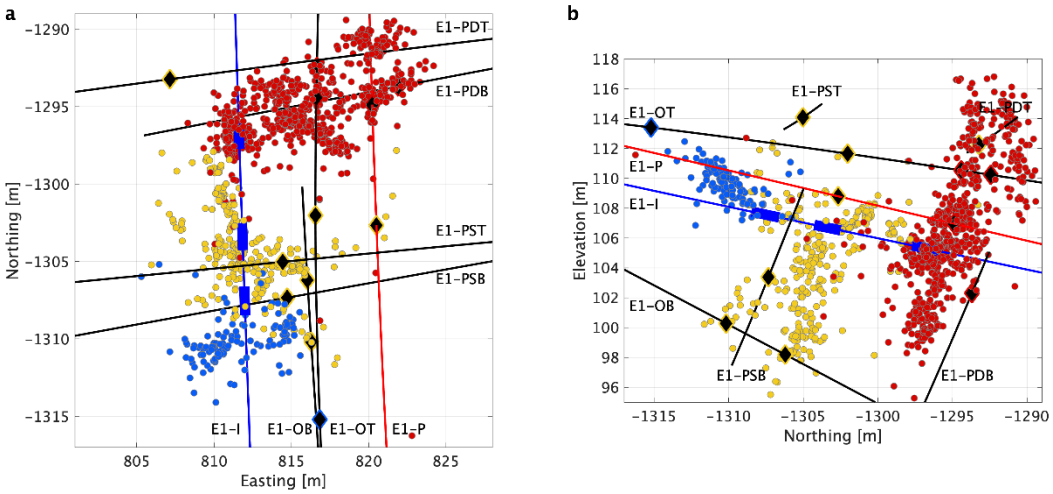

Figure 11: Seismic activity from stimulations between May and December, 2018. Events are colored based on the injection interval where injection occurred. Red is the 164 ft interval, yellow the 142 ft interval and blue the 128 ft interval. Thick blue segments of E1-I mark the extent of the three injection intervals. Black diamonds are locations of temperature anomalies detected by the DTS system during the flow tests as a result of fracturing and associated fluid flow.

4.1. DTS and E1-P intercepts

Multiple thermal anomalies were detected in the monitoring boreholes during fluid injection. All of them were positive anomalies in the 0.3 – 1.0 K range. Usually, the closest seismicity was found within 1 m, i.e. the determined range of location uncertainty. Additionally, downhole camera video obtained in E1-P identified fluid inflow at several locations at ~38 m depth in E1-P during injection at the 164 ft location and at ~31.0 m depth in E1-P during injection at the 142 ft location of E1-I. These observations independently confirm the location accuracy of the seismic monitoring system as discussed above and shown in Figure 3.

It appears that for several of the recorded thermal anomalies, fracture propagation stopped at the boreholes indicating that they strongly influence the local hydraulic regime and inhibit further seismic activity. For example, during the Dec 20 & 21 injections, fractures hit the boreholes E1-OB at two locations, and E1-PSB at a single location but did not continue migrating past these intercept locations. These boreholes intersections are interpreted to have acted as 'pressure relief' points, in agreement with the observed thermal anomalies from the Joule-Thomson effect as pressure decreased; inhibiting further fracture growth (Figure 11). These observations are in agreement with pre-stimulation modeling results and based on lab-scale experiments (Frash et al., 2018, 2020), and suggest that production boreholes should not be drilled prior to stimulations unless a dual stimulation, where injection and production boreholes are pressurized simultaneously, is planned. Any borehole will act as pressure relief as soon as it

is connected to the fracture network, even with very small permeability or applied back pressure. In order to create a high permeability connection, the rock beyond the borehole needs to be stimulated as well to connect further natural fractures. This can only be achieved if no pressure sink, such as a borehole, is available close by.

During the July 21 and December 20 & 21 tests significant reactivation occurred on pre-existing structures. Although no seismicity reached the monitoring boreholes we recorded thermal anomalies in agreement with the observed trends of seismic activity. These were observed in E1-OB on July 21 and in E1-PDT and E1-PST on Dec 20 (Figure 11). It appears that fracture propagation may occur ahead of the front of detectable seismic activity. This may be a network bias with seismicity close to boreholes implicitly also being at the edge of the seismic network where detection levels are worse. It may also indicate that aseismic deformation drives these fractures. This advancement of fracture flow beyond the seismically active region has not been observed for the created hydraulic fractures.

4.2. Velocity model

To further characterize the 3-D volume, we performed a tomographic inversion using tomoDD (Zhang & Thurber, 2003) and using P-wave travel times only to determine an isotropic 3-D velocity model. With the seismic catalog obtained from Hypoinverse, we are able to constrain seismic velocity variations around the seismically active volume. The resulting 3-D velocity model has an average P-wave velocity of 5,873 m/s with a standard deviation of 594 m/s (Figure 12); this average value is very similar to P-wave velocity (5900 m/s) used for our simplified model. The average P-wave velocity agrees with that obtained from minimizing the differences between known and determined locations of CASSM sources. Given an average P-wave travel time of 3 milliseconds, the location error would be around one meter if we used a P-wave velocity that is one standard deviation away from the average instead of the average velocity. This interpretation is consistent with the location uncertainty derived above based on (1) the active sources and (2) the formal uncertainty given by the residual of each determined event location.

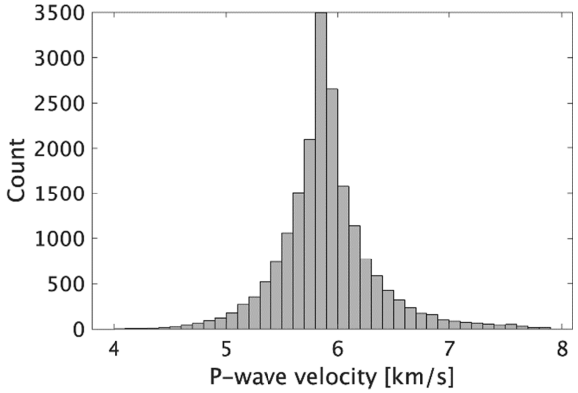

Figure 12: Distribution of P-wave velocity as obtained from tomoDD tomography.

4.3. Fracture network

The injection tests at the three locations in E1-I produced seismicity having a wide variety of fracture orientations highlighting the importance of the natural rock fabric (foliation, bedding planes, pre-existing fractures, and structural heterogeneity) for fracture propagation. To understand the reactivation mechanism of the identified fracture planes we compute the slip tendency in the unperturbed stress field (Morris et al., 1996). The slip tendency T is defined as the ratio of shear stress τ to normal stress σ_n acting on a potential slip surface, $T = \tau/\sigma_n$. It is a relative measure of how likely a fault of a given orientation is to slip in a given stress field. The assumed stress magnitudes are 41.8 MPa for the vertical stress, a minimum horizontal stress of 21.7 MPa and a maximum horizontal stress of 34.0 MPa with an orientation of N92˚E (Singh et al., 2019; Dobson et al., 2020). The slip tendency is plotted along with the interpreted fractures in Figure 13. Of all the reactivated fracture planes, only F9 appears to be well oriented for shear slip. Fractures F1, F3, F4, and F10 are oriented consistently about 22˚ east of the assumed S_{Hmax} direction. This difference is at the upper range of expected variation of the stress orientation at SURF and other sites with crystalline rock (Schoenball & Davatzes, 2017). Thus, these fractures are compatible with the concept of hydraulic fractures. We do note the location of fractures F1, F3, and F4 detached from the other activated fractures which are clear indications of discontinuities during the fracture propagation (Figure 5). Particularly fractures F3 and F4 appear to be sub-parallel strands of hydraulic fractures about 1 m apart. This suggests that hydraulic fractures grow until they hit a hydraulically active natural fracture where they may abut, with a step-over through the pre-existing fracture until a flow barrier is hit, which would then promote the creation of a new hydraulic fracture. This has been directly observed e.g. in mine-back experiments described by Jeffrey et al. (2009).

Although fracture F1 does fit the orientation of a hydraulic fracture, its detached location, vigorous seismic activity and in particular the persisting seismic activity after shut-in that occurred repeatedly draws some doubt to this interpretation. These types of seismogenic responses are usually associated with critically stressed faults (Schoenball, 2019). Hydraulic fractures on the other hand are expected to be purely driven by fluid injection and would cease to propagate once the fluid injection has stopped. Indeed, seismicity quickly ceased on all of the other activated fractures after shut-in. However, this type of behavior has been observed in a number of EGS field sites, such as Soultz-sous-Forêts, Basel, and the Cooper Basin, and has been interpreted to represent ongoing pressure diffusion following cessation of injection (e.g., Baisch et al., 2010; Baisch & Vörös, 2010).

Fractures F2 and F6 form off-shoots from the main trend of activity of the 164 ft injection and are of similar orientation as fracture F7 activated during the 142 ft injection. They are oriented more favorably for shearing but are still far from optimally oriented for slip. These fractures would be well oriented for failure for lower magnitudes of S_{Hmax} and a stress regime approaching strike-slip. It is likely

that these fractures were pre-existing and reactivated in shear, once they were intersected by the hydraulic fracture.

Fractures F5 and F6 were activated during injections at 128 ft and have a very different orientation to the previously discussed fractures. Based on the stress field information, they would have the lowest slip tendency of all interpreted fractures. This is consistent with the highest pressures that were observed during the fracture propagation stage.

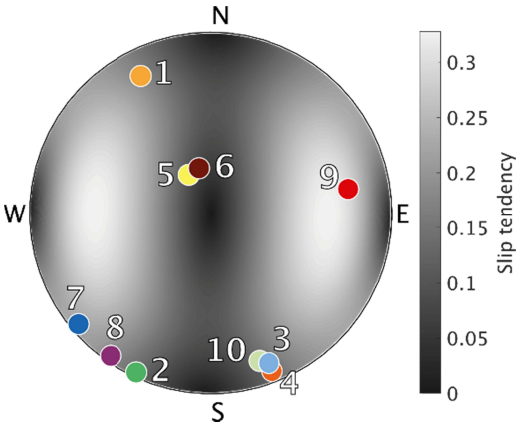

Figure 13: Slip tendency and fracture poles in lower hemisphere projection. Colors of fracture normals are the same as in Figure 5.

The identified fractures show strongly varying seismic response with some features showing dense seismicity such as F9 while others are poorly defined through the seismicity but a independently confirmed through fracture intersections will boreholes, such as F10. In the following we attempt to quantify the different seismic response for each single fracture.

Induced seismicity is caused by elevated fluid pressure and changes of the effective stress. However, during ongoing stimulation and after fracturing has been initiated it is the injected fluid volume that continues to drive sustained seismic activity. For each fracture, we compute the volume of fluid injected during the time between two consecutive detected events that were associated with that fracture. We only account consecutive events that occurred during the same injection period. We obtained a distribution of inter-event volume for each fracture. Variations in the inter-event volume can then be interpreted either as resulting from the hydraulic conditions of the fracture network (e.g. favoring fluid flow into certain features) or as resulting from the varying seismogenic potential of a given feature (e.g. a higher density of critically stressed asperities). For the first interpretation the hydraulic regime defined by all fractures and the rock matrix favors certain fractures and promotes fluid flow that leads to seismicity. Fractures that receive the majority of fluid would have a small inter-event volume, while fractures that receive less fluid

would have a large inter-event volume as most of the injected fluid by-passes them. In the second interpretation, small inter-event volume represents critically-stress fractures in the sense that many asperities exist that rupture seismically under the applied hydraulic conditions. Large inter-event volume would then correspond to a low density of critically stressed asperities and vice versa.

Figure 14 shows the distributions of inter-event volume for all fractures. We obtain inter-event volumes spanning more than two orders of magnitude. For most the median inter-event volume was between 2 and 12 L. Outliers were F1 and F9 with significantly smaller median inter-event volumes of 0.8 and 0.2 L, respectively. F10 had a significantly larger median inter-event volume of 38 L. F1 had the same strike of hydraulic fractures F3, F4, and F10 but an opposite dip direction. Based on slip tendency (Figure 13), it should still have very similar geomechanical conditions as the other hydraulic fractures. However, the persisting seismic activity in this fracture after the second May 25 flow test indicated that this fracture may have a higher seismogenic potential than the other features.

Shear fracture F9 has the highest slip tendency of all identified fractures (Figure 13), which is consistent with the smallest inter-event volume (Figure 14). The large inter-event volume exhibited by F10 can be explained by the strong seismic activity simultaneously occurring in F7. It is conceivable that F7 dominated the hydraulic regime during this injection test and only marginal amounts of fluid were driving the propagation of the new hydraulic fracture F10, resulting in little overall seismic activity.

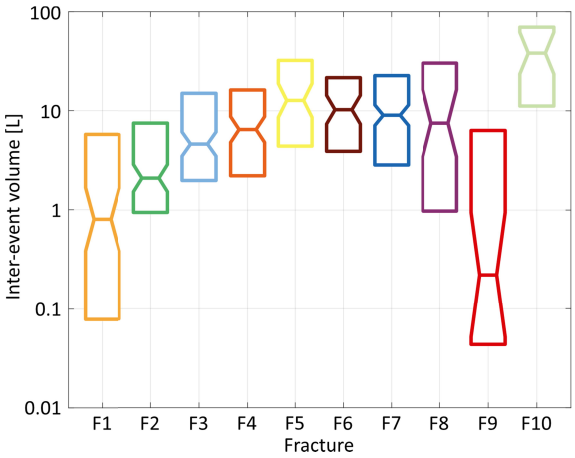

Figure 14: Boxplots of the distributions of inter-event volume calculated for each fracture [F1-F10, number of events (top axis)]. Horizontal lines represent the second quartile, median and third quartile value, respectively. Two medians are significantly different at 95% confidence if the notched intervals do not overlap.

4.4. General observations and comparison to other sites

The seismic activity of mesoscale hydraulic fracturing and shear activation in crystalline rock has now been studied at the Äspö, Grimsel, and Sanford underground laboratories (Gischig et al., 2018; Villiger et al., 2019; Zang et al., 2017; and this study). For all of these experiments, borehole sections of 0.5 to 2 m were isolated using straddle packers. One-sided fracture zones or hydraulic fractures, i.e. fractures growing unilaterally from the injection well, were activated in almost all fracture stages during these experiments. For our experiment thermal stress gradients could explain the preferential growth towards the mine drift that was observed for most structures (Fu et al., 2018). However, this phenomenon was also observed for reactivation of pre-existing fractures and with fracture propagation away from the drift, such as for fracture F9. At Äspö and Grimsel fracture growth does not seem to follow a systematic trend. There one-sided fractures were observed to grow towards or away from the closest galleries or drifts. Together these observations suggest that the local conditions at the borehole wall crucially determine the course of a stimulation treatment. The first nucleation point of substantial fracture growth appears to determine the trajectory a propagating fracture may take. This interpretation is in line with the concept of channelized fluid flow and heterogeneous pore fluid pressure fields in rough-walled fractures (Auradou et al., 2006; Marchand et al., 2019).

Similar observations that the majority of seismicity does occur away from the injection borehole, rather than centered on the well, have been made similarly at full scale at Soultz-sous-Forêts (Dorbath et al., 2009). There, highest event rates occurred in a zone about 200 m away from the injection well. At Pohang, Korea earlier seismicity on the fault plane that produced the M5.4 event also occurred at a significant distance from the injection well (Ellsworth et al., 2019) and was not centered on the injection borehole.

Another interesting observation was the presence of multi-strand hydraulic fractures that were produced from the same injection interval and run sub-parallel. As has been directly observed by Jeffrey et al., (2009) through a mine-back experiment it seems that hydraulic fractures may abut against natural fractures and initiate a new hydraulic fracture after making a step-over. This is again an observation that highlights the important role that pre-existing structures play. Numerical modelling schemes that strive to represent fracture stimulation in crystalline rock need to include such fracture interactions.

Our injection experiments were designed to create hydraulic fractures rather than activate pre-existing features through shear. Since the rock mass is ubiquitously fractured we were not able to find injection intervals that are free of weaknesses such as fractures, quartz inclusions, foliation and bedding planes in the metamorphic rock. As a consequence, the hydraulic stimulations produced significant levels of shear reactivation. Still, we were able to create hydraulic fractures as well. For injections at the 164 ft location hydraulic fractures appear to dominate the seismic response. The dominant source for shear reactivation was fracture F2, which was intersected by the hydraulic fracture about 3 m away from E1-I.

At that point the hydraulic fracture was already well-developed and its propagation was not significantly disturbed by the adjacent shear activation. For the 142 ft injection the reactivated shear fracture originates at the injection interval. Hence, the seismic activity in this feature is vigorous and presumably also channeled most of the fluid flow away from the hydraulic fracture. As a result, only minor seismic activity was observed in F10. Subsequent flow testing at the 142 ft location did not reveal significant hydraulic connectivity between E1-I and E1-P. This suggests that the shear reactivation inhibited hydraulic fracture growth.

During this stimulation period parts of the activated and newly created fractures intersected a total of five monitoring boreholes. The thermal anomalies detected in the monitoring boreholes indicate a pressure reduction as water flowed from the fractures into the (partially) grouted boreholes. In most instances fracture propagation stopped along the direction of the fracture intercept, presumably as a response to this pressure reduction.

5. Conclusions

We have measured the seismic activity associated with mesoscale hydraulic fracturing tests utilizing a novel 100 kHz, continuous seismic monitoring system deployed in six monitoring boreholes surrounding the experimental domain in 3-D. The multi-modal data that were recorded at several stages of the experiment provided extremely useful complementary constraints that helped to validate the image obtained from the passive seismic monitoring.

Despite the high seismic Q properties of the rock the signal-to-noise ratio achieved by the accelerometers proved challenging to analyze. We were able to locate a total of 1933 seismic events during several injection periods at three locations of the injection borehole E1-I. Our seismicity locations were confirmed through locating known active sources as well as independently through 12 fracture intercepts in all monitoring boreholes recorded with the DTS system and observed fluid inflow in E1-P. When propagating fractures intersected boreholes, the boreholes (grouted or not) appeared to act as pressure relief points that arrested fracture growth.

For two injection intervals we were able to create hydraulic fractures. In all intervals, however, we observed significant shear activation of pre-existing structures. Although the geometry of the hydraulic fractures may be complex, including branching into parallel strands and step-overs, the two main hydraulic fractures are remarkably parallel intersecting each of the boreholes E1-I, E1-OT and E1-P at locations 12 m apart. One-sided fractures and heterogeneity of stress dictate the outcome of hydraulic stimulations. This is still the case when stimulation attempts to rely on theoretically well-behaved hydraulic fractures that develop parallel to S_{Hmax} in an idealized system.

Once fractures were intersected by boreholes, the boreholes acted as a pressure relief and fracture propagation ceased, consistent with pre-stimulation modelling. Further, when a fracture only grows to a production borehole and stops its propagation there, the aperture of this new hydraulic connection would not be very large. This would further limit the created hydraulic connectivity between injection and production boreholes. Likewise, because a fracture connection has already been made between the boreholes, it may be difficult to further create a good hydraulic fracture connection by reversing the flow direction (i.e., inject into the production well) after the fracture has been created. This suggests that in order to create a good hydraulic communication between injection and production boreholes, the latter should not be drilled before the end of a stimulation.

Acknowledgements

This material was based upon work supported by the U.S. Department of Energy, Office of Energy Efficiency and Renewable Energy (EERE), Office of Technology Development, Geothermal Technologies Office, under Award Number DE-AC52-07NA27344 with LLNL, and Award Number DE-AC02-05CH11231 with LBNL. The United States Government retains, and the publisher, by accepting the article for publication, acknowledges that the United States Government retains a non-exclusive, paid-up, irrevocable, world-wide license to publish or reproduce the published form of this manuscript, or allow others to do so, for United States Government purposes.

This manuscript has been authored in part by UT-Battelle, LLC, under contract DE-AC05-00OR22725 with the US Department of Energy (DOE). DOE will provide public access to these results of federally sponsored research in accordance with the DOE Public Access Plan (http://energy.gov/downloads/doe-public-access-plan).

The research supporting this work took place in part at the Sanford Underground Research Facility in Lead, South Dakota. The assistance of the Sanford Underground Research Facility and its personnel in providing physical access and general logistical and technical support is acknowledged. We thank Grzegorz Kwiatek and Katrin Plenkers for helpful discussion. The seismic data discussed here is available in Schoenball et al. (2019).

This paper describes objective technical results and analysis. Any subjective views or opinions that might be expressed in the paper do not necessarily represent the views of the U.S. Department of Energy or the United States Government.

References

Allen, R. V. (1978). Automatic Earthquake Recognition and Timing from Single Traces. *Bulletin of the Seismological Society of America*, *68*(5), 1521–1532.

Amann, F., Gischig, V., Evans, K., Doetsch, J., Jalali, R., Valley, B., et al. (2018). The seismo-hydromechanical behavior during deep geothermal reservoir stimulations: open questions tackled in a decameter-scale in situ stimulation experiment. *Solid Earth*, *9*(1), 115–137. doi:10.5194/se-9-115-2018

Auradou, H., Drazer, G., Boschan, A., Hulin, J.-P., & Koplik, J. (2006). Flow channeling in a single fracture induced by shear displacement. *Geothermics*, *35*(5–6), 576–588. doi:10.1016/j.geothermics.2006.11.004

Baisch, S., Vörös, R., Rothert, E., Stang, H., Jung, R., and Schellschmidt, R. (2010) A numerical model for fluid injection induced seismicity at Soultz-sous-Forêts. *International Journal of Rock Mechanics & Mining Sciences*, 47, 405-413. doi: 10.1016/j.ijrmms.2009.10.001.

Baisch, S., and Vörös, R. (2010). Reservoir induced seismicity: Where, when, why and how strong. *Proceedings World Geothermal Congress 2010*, 5 p.

Caddey, S. W., Bachman, R. L., Campbell, T. J., Reid, R. R., & Otto, R. P. (1991). The Homestake gold mine, an early Proterozoic iron-formation-hosted gold deposit, Lawrence County, South Dakota. In *U.S. Geological Survey Bulletin 1857-J, Geology and resources of gold in the United States* (p. 67). doi:10.3133/b1857J

Chen, C., & Holland, A. A. (2016). PhasePApy: A Robust Pure Python Package for Automatic Identification of Seismic Phases. *Seismological Research Letters*, *87*(6), 1384–1396. doi:10.1785/0220160019

Daley, T. M., Solbau, R. D., Ajo-Franklin, J. B., & Benson, S. M. (2007). Continuous active-source seismic monitoring of CO_2 injection in a brine aquifer. *GEOPHYSICS*, *72*(5), A57–A61. doi:10.1190/1.2754716

Diehl, T., Kraft, T., Kissling, E., & Wiemer, S. (2017). The induced earthquake sequence related to the St. Gallen deep geothermal project (Switzerland): Fault reactivation and fluid interactions imaged by microseismicity. *Journal of Geophysical Research: Solid Earth*, *122*(9), 7272–7290. doi:10.1002/2017JB014473

Dobson, P., Kneafsey, T.J., Blankenship, D., Morris, J., Fu, P., Knox, H., et al. (2020) The EGS Collab Project - Fracture stimulation and flow experiments for coupled process model validation at the Sanford Underground Research Facility (SURF), South Dakota, USA. *Proceedings World Geothermal Congress 2020*, 13 p.

Doe, T., McLaren, R., and Dershowitz, W. (2014). Discrete Fracture Network Simulations of Enhanced Geothermal Systems. In *Proceedings 39th Workshop on Geothermal Reservoir Engineering, Stanford University*, 11 p.

Dorbath, L., Cuenot, N., Genter, A., & Frogneux, M. (2009). Seismic response of the fractured and

faulted granite of Soultz-sous-Forets (France) to 5 km deep massive water injections. *Geophysical Journal International*, 177(2), 653–675. doi:10.1111/j.1365-246X.2009.04030.x

Dresen, G., Renner, J., Bohnhoff, M., Konietzki, H., Kwiatek, G., Plenkers, K., Klee, G., & Backers, T. (2019). STIMTEC - a mine-back experiment in the Reiche Zeche underground laboratory. EGU2019-9357, In *Proceedings 21st EGU General Assembly*, Vienna, Austria.

Ellsworth, W. L., Giardini, D., Townend, J., Ge, S., & Shimamoto, T. (2019). Triggering of the Pohang, Korea, Earthquake (Mw 5.5) by Enhanced Geothermal System Stimulation. *Seismological Research Letters*. doi:10.1785/0220190102

Frash, L. P., Carey, J. W., Welch, N. J., & EGS Collab Team. (2019). EGS Collab Experiment 1 Geomechanical and Hydrological Properties by Triaxial Direct Shear. In *Proceedings 44th Workshop on Geothermal Reservoir Engineering, Stanford University*. 11 p.

Frash, L.P., Fu, P., Morris, J., and EGS Collab Team. (2018) Fracture caging: Can we control the extent of a hydraulic fracture stimulated zone? In *Proceedings 43rd Workshop on Geothermal Reservoir Engineering, Stanford University,* 8 p.

Frash, L. P., J. C. Hampton, M. S. Gutierrez, and E. C. Team (2020), Fracture Caging to Control Induced Seismicity with Inspiration from the EGS Collab Project, In *Proceedings 45th Workshop on Geothermal Reservoir Engineering*, p. 10, Stanford University, Stanford, California.

Fu, P., White, M. D., Morris, J. P., Kneafsey, T. J., & EGS Collab Team. (2018). Predicting Hydraulic Fracture Trajectory Under the Influence of a Mine Drift in EGS Collab Experiment I. In *Proceedings 43rd Workshop on Geothermal Reservoir Engineering, Stanford University,* 11 p.

Gao, K., Huang, L., Knox, H. A., Schwering, P. C., Hoots, C. R., Ajo-Franklin, J., Kneafsey, T., and the EGS Collab Team (2020). Anisotropic Elastic Properties of the First EGS Collab Testbed Revealed from the Campaign Cross-Borehole Seismic Data. In *Proceedings 45th Workshop on Geothermal Reservoir Engineering, Stanford University*, 11 p.

Genter, A., Evans, K. F., Cuenot, N., Fritsch, D., & Sanjuan, B. (2010). Contribution of the exploration of deep crystalline fractured reservoir of Soultz to the knowledge of enhanced geothermal systems (EGS). *Comptes Rendus Geoscience*, *342*(7–8), 502–516. doi:10.1016/j.crte.2010.01.006

Gischig, V. S., Doetsch, J., Maurer, H., Krietsch, H., Amann, F., Evans, K. F., et al. (2018). On the link between stress field and small-scale hydraulic fracture growth in anisotropic rock derived from microseismicity. *Solid Earth*, *9*(1), 39–61. doi:10.5194/se-9-39-2018

Grant, M.A. (2016). Physical performance indicators for HDR/EGS projects. *Geothermics*, 63, 2-4, doi:10.1016/j.geothermics.2015.01.004

Guglielmi, Y., Cappa, F., Lançon, H., Janowcsyk, J. B., Rutqvist, J., Tsang, C.-F., & Wang, J. S. Y. (2014). ISRM Suggested Method for Step-Rate Injection Method for Fracture In-Situ Properties

(SIMFIP): Using a 3-Components Borehole Deformation Sensor. *Rock Mechanics and Rock Engineering*, *47*(1), 303–311. doi:10.1007/s00603-013-0517-1

Häring, M. O., Schanz, U., Ladner, F., & Dyer, B. C. (2008). Characterisation of the Basel 1 enhanced geothermal system. *Geothermics*, *37*(5), 469–495. doi:10.1016/j.geothermics.2008.06.002

Heise, J. (2015). The Sanford Underground Research Facility at Homestake. Journal of Physics: Conference Series, v. 606 (1), *IOP Publishing*, 25 p., doi:10.1088/1742-6596/606/1/012015

Ingraham, M. D., King, D. K., Knox, H. A., Strickland, C. E., Vermeul, V. R., Guglielmi, Y., et al. (2018). Design of a Long Term Hydraulic Fracture and Flow System. *52nd U.S. Rock Mechanics/Geomechanics Symposium*. Seattle, Washington: American Rock Mechanics Association, ARMA 18-0130, 7 p.

Jeffrey, R. G., Bunger, A., LeCampion, B., Zhang, X., Chen, Z., van As, A., et al. (2009). Measuring Hydraulic Fracture Growth in Naturally Fractured Rock. In *SPE Annual Technical Conference and Exhibition* (p. SPE 124919). Society of Petroleum Engineers. doi:10.2118/124919-MS

Johnson, T., Strickland, C., Knox, H., Thomle, J., Vermeul, V., Ulrich, C., Kneafsey, T,, et al. (2019). EGS Collab Project Electrical Resistivity Tomography Characterization and Monitoring. In *Proceedings 44th Workshop on Geothermal Reservoir Engineering, Stanford University*, 8 p.

Jung, R. (2013). EGS - goodbye or back to the future. In R. Jeffrey (Ed.), *Effective and Sustainable Hydraulic Fracturing*. InTech. doi:10.5772/45724

Klein, F. W. (2014). *User's Guide to HYPOINVERSE-2000, a Fortran Program to Solve for Earthquake Locations and Magnitude* (U. S. Geological Survey, Open File Report 02-171, revised June 2014).

Kneafsey, T. J., Blankenship, D., Knox, H. A., Johnson, T. C., Ajo-Franklin, J. B., Schwering, P. C., et al. (2019). EGS Collab Project: Status and Progress. In *Proceedings 44th Workshop on Geothermal Reservoir Engineering, Stanford University*, 16 p.

Krischer, L., Megies, T., Barsch, R., Beyreuther, M., Lecocq, T., Caudron, C., & Wassermann, J. (2015). ObsPy: a bridge for seismology into the scientific Python ecosystem. *Computational Science & Discovery*, *8*(1), 014003. doi:10.1088/1749-4699/8/1/014003

Kwiatek, G, Plenkers, K., & Dresen, G. (2011). Source Parameters of Picoseismicity Recorded at Mponeng Deep Gold Mine , South Africa : Implications for Scaling Relations. *Bulletin of the Seismological Society of America*, *101*(6), 2592–2608. doi:10.1785/0120110094

Kwiatek, G., Martínez-Garzón, P., Plenkers, K., Leonhardt, M., Zang, A., von Specht, S., et al. (2018). Insights Into Complex Subdecimeter Fracturing Processes Occurring During a Water Injection Experiment at Depth in Äspö Hard Rock Laboratory, Sweden. Journal of Geophysical Research: Solid Earth, 123, 6616–6635. doi:10.1029/2017JB014715

Linneman, D., Knox, H., Schwering, P., and Hoots, C., (2018). The EGS Collab Hydrofracture

Experiment at the Sanford Underground Research Facility – Campaign Cross-Borehole Seismic Characterization. *AGU Fall Meeting*, Washington, D.C.

Marchand, S., Mersch, O., Selzer, M., Nitschke, F., Schoenball, M., Schmittbuhl, J., et al. (2019). A Stochastic Study of Flow Anisotropy and Channelling in Open Rough Fractures. *Rock Mechanics and Rock Engineering*. doi:10.1007/s00603-019-01907-4

McClure, M. W., & Horne, R. N. (2014). An investigation of stimulation mechanisms in Enhanced Geothermal Systems. *International Journal of Rock Mechanics and Mining Sciences*, *72*, 242–260. doi:10.1016/j.ijrmms.2014.07.011

Morris, A., Ferrill, D. A., & Brent Henderson, D. B. (1996). Slip-tendency analysis and fault reactivation. *Geology*, *24*(3), 275. doi:10.1130/0091-7613(1996)024<0275:STAAFR>2.3.CO;2

Morris, J. P., Dobson, P. F., Knox, H. A., Ajo-Franklin, J. B., White, M. D., Fu, P., et al. (2018). Experimental Design for Hydrofracturing and Fluid Flow at the DOE Collab Testbed. In *Proceedings 43rd Workshop on Geothermal Reservoir Engineering, Stanford University,* 9 p.

Neupane, G., Podgorney, R. K., Huang, H., Mattson, E. D., Kneafsey, T. J., Dobson, P. F., et al. (2019). EGS Collab Earth Modeling: Integrated 3D Model of the Testbed. *GRC Transactions*, *43*, 22 p.

Norbeck, J. H., McClure, M. W., & Horne, R. N. (2018). Field observations at the Fenton Hill enhanced geothermal system test site support mixed-mechanism stimulation. *Geothermics*, *74*, 135–149. doi:10.1016/J.GEOTHERMICS.2018.03.003

Oldenburg, C. M., Dobson, P. F., Wu, Y., Cook, P., Kneafsey, T. J., Nakagawa, S., et al. (2017). Hydraulic Fracturing Experiments at 1500 m Depth in a Deep Mine: Highlights from the kISMET Project. In *Proceedings 42nd Workshop on Geothermal Reservoir Engineering, Stanford University,* 9 p.

Parker, R. (1999). The Rosemanowes HDR project 1983-1991. *Geothermics*, *28*(4–5), 603–615.

Roggenthen, W. M., Doe, T. W., & the EGS Collab team (2018). Natural Fractures and Their Relationship to the EGS Collab Project in the Underground of the Sanford Underground Research Facility (SURF). In *52nd US Rock Mechanics / Geomechanics Symposium, Seattle*, ARMA 18-1190, 11 p.

Schoenball, M., & Davatzes, N. C. (2017). Quantifying the heterogeneity of the tectonic stress field using borehole data. *Journal of Geophysical Research: Solid Earth*, *122*(8), 6737–6756. doi:10.1002/2017JB014370

Schoenball, M. (2019) Clustering in fluid-induced seismicity and what it tells us about its source. In *SEG Annual Meeting 2019*, San Antonio, Texas, doi:10.1190/segam2019-3215187.1.

Schoenball, M., Ajo-Franklin, J. B., Robertson, M., Wood, T., Blankenship, D., Cook, P., et al. (2019). *EGS Collab Experiment 1: Microseismic Monitoring*. doi:10.15121/1557417

Singh, A., Zoback, M., Neupane, G., Dobson, P. F., Kneafsey, T.J., Schoenball, M. et al. (2019). Slip Tendency Analysis of Fracture Networks to Determine Suitability of Candidate Testbeds for the EGS Collab Hydroshear Experiment. *GRC Transactions, 43*, 20 p.

Tester, J.W., Blackwell, D., Petty, S., Richards, M., Moore, M.C., Anderson, B., Livesay, B., Augustine, C., DiPippo, R., Nichols, K., Veatch, R., Drake, E., Toksoz, N., Baria, R., Batchelor, A.S., Garnish, J. (2006). The future of geothermal energy: An assessment of the energy supply potential of engineered geothermal systems (EGS) for the United States. *Massachusetts Institute of Technology*, INL/EXT-06-11746, ISBN: 0-615-13438-6.

Ulrich, C., Dobson, P. F., Kneafsey, T. J., Roggenthen, W. M., Uzunlar, N., Doe, T. W., et al. (2018). The distribution, orientation, and characteristics of natural fractures for Experiment 1 of the EGS Collab Project, Sanford Underground Research Facility. In *52nd US Rock Mechanics / Geomechanics Symposium, Seattle*, ARMA 18-1252, 8 p.

Vigilante, P. J., Sone, H., Wang, H. F., Haimson, B., & Doe, T. W. (2017). Anisotropic Strength of Poorman Formation Rocks, kISMET Project. In *51st US Rock Mechanics / Geomechanics Symposium*. San Franscisco, California, USA: American Rock Mechanics Association, ARMA 2017–0766, 6 p.

Villiger, L., Gischig, V. S., Doetsch, J., Krietsch, H., Dutler, N. O., Jalali, M. R., et al. (2019). Influence of reservoir geology on seismic response during decameter scale hydraulic stimulations in crystalline rock. *Solid Earth*. doi:10.5194/se-2019-159

Walsh, F. R., & Zoback, M. D. (2016). Probabilistic assessment of potential fault slip related to injection-induced earthquakes: Application to north-central Oklahoma, USA. *Geology*, *44*(12), 991–994. doi:10.1130/G38275.1

Wang, H. F., Lee, M. Y., Doe, T., Haimson, B. C., Oldenburg, C. M., & Dobson, P. F. (2017). In-situ stress measurement at 1550-meters depth at the kISMET test site in Lead, S.D. In *51st US Rock Mechanics / Geomechanics Symposium*. San Franscisco, California, USA: American Rock Mechanics Association, ARMA 2017–0651, 7 p.

White, M. D., P. Fu, A. Ghassemi, H. Huang, J. Rutqvist, B. Johnston, and EGS Collab Team (2018), Numerical Simulation Applications in the Design of EGS Collab Experiment 1, In *Proceedings 43rd Workshop on Geothermal Reservoir Engineering, Stanford University*, Stanford, California.

Zang, A., Stephansson, O., Stenberg, L., Plenkers, K., Specht, S., Milkereit, C., et al. (2017). Hydraulic fracture monitoring in hard rock at 410 m depth with an advanced fluid-injection protocol and extensive sensor array. *Geophysical Journal International*, *208*(2), 790–813. doi:10.1093/gji/ggw430

Zhang, H., & Thurber, C. H. (2003). Double-Difference Tomography: The Method and Its Application to

the Hayward Fault, California. *Bulletin of the Seismological Society of America*, *93*(5), 1875–1889. doi:10.1785/0120020190

Zhang, Y., Doughty, C., Pan, L., Kneafsey, T. J., & the EGS Collab team (2018). What Could We See at The Production Well Before The Thermal Breakthrough? In *Proceedings 43rd Workshop on Geothermal Reservoir Engineering, Stanford University*, 4 p., Stanford, California.